

Redox-driven mineral and organic associations in Jezero Crater, Mars

<https://doi.org/10.1038/s41586-025-09413-0>

Received: 13 November 2024

Accepted: 15 July 2025

Published online: 10 September 2025

Open access

 Check for updates

Joel A. Hurowitz^{1✉}, M. M. Tice², A. C. Allwood³, M. L. Cable³, K. P. Hand³, A. E. Murphy⁴, K. Uckert³, J. F. Bell III⁵, T. Bosak⁶, A. P. Broz⁷, E. Clavé⁸, A. Cousin⁹, S. Davidoff³, E. Dehouck¹⁰, K. A. Farley¹¹, S. Gupta¹², S.-E. Hamran¹³, K. Hickman-Lewis¹⁴, J. R. Johnson¹⁵, A. J. Jones¹², M. W. M. Jones^{16,17}, P. S. Jørgensen¹⁸, L. C. Kah¹⁹, H. Kalucha¹¹, T. V. Kizovski²⁰, D. A. Klevang¹⁸, Y. Liu³, F. M. McCubbin²¹, E. L. Moreland²², G. Paar²³, D. A. Paige²⁴, A. C. Pascuzzo²⁵, M. S. Rice²⁶, M. E. Schmidt²⁰, K. L. Siebach²², S. Siljeström²⁷, J. I. Simon²¹, K. M. Stack³, A. Steele²⁸, N. J. Tosca²⁹, A. H. Treiman³⁰, S. J. VanBommel³¹, L. A. Wade³, B. P. Weiss⁶, R. C. Wiens⁷, K. H. Williford³², R. Barnes¹², P. A. Barr²⁵, A. Bechtold³³, P. Beck³⁴, K. Benzerara³⁵, S. Bernard³⁶, O. Beyssac³⁷, R. Bhartia³⁸, A. J. Brown³⁹, G. Caravaca^{9,40}, E. L. Cardarelli²⁴, E. A. Cloutis⁴¹, A. G. Fairén⁴², D. T. Flannery⁴³, T. Fornaro⁴⁴, T. Fouchet⁴⁵, B. Garczynski²⁶, F. Gómez⁴², E. M. Hausrath⁴⁶, C. M. Heirwegh³, C. D. K. Herd⁴⁷, J. E. Huggett²⁵, J. L. Jørgensen¹⁸, S. W. Lee³, A. Y. Li⁴⁸, J. N. Maki³, L. Mandon^{11,49}, N. Mangold⁵⁰, J. A. Manrique⁵¹, J. Martínez-Frías⁵², J. I. Núñez¹⁵, L. P. O'Neil², B. J. Orenstein⁴³, N. Phelan²⁵, C. Quantin-Nataf¹⁰, P. Russell²⁴, M. D. Schulte⁵³, E. Scheller⁶, S. Sharma²⁸, D. L. Shuster⁵⁴, A. Srivastava²⁸, B. V. Wogoland¹⁹ & Z. U. Wolf⁵⁵

The Perseverance rover has explored and sampled igneous and sedimentary rocks within Jezero Crater to characterize early Martian geological processes and habitability and search for potential biosignatures^{1–7}. Upon entering Neretva Vallis, on Jezero Crater's western edge⁸, Perseverance investigated distinctive mudstone and conglomerate outcrops of the Bright Angel formation. Here we report a detailed geological, petrographic and geochemical survey of these rocks and show that organic-carbon-bearing mudstones in the Bright Angel formation contain submillimetre-scale nodules and millimetre-scale reaction fronts enriched in ferrous iron phosphate and sulfide minerals, likely vivianite and greigite, respectively. This organic carbon appears to have participated in post-depositional redox reactions that produced the observed iron-phosphate and iron-sulfide minerals. Geological context and petrography indicate that these reactions occurred at low temperatures. Within this context, we review the various pathways by which redox reactions that involve organic matter can produce the observed suite of iron-, sulfur- and phosphorus-bearing minerals in laboratory and natural environments on Earth. Ultimately, we conclude that analysis of the core sample collected from this unit using high-sensitivity instrumentation on Earth will enable the measurements required to determine the origin of the minerals, organics and textures it contains.

NASA's Mars 2020 Perseverance rover mission is the first in a sequence of missions designed to return a scientifically selected suite of Martian rock, regolith and atmosphere samples to Earth for laboratory investigation. The goals of the mission are to explore the Jezero Crater landing site and its surroundings, constrain the geologic history and habitability of the site, seek signs of past life, and prepare a cache of samples for potential return to Earth¹. The Perseverance rover carries an instrument payload designed to fulfil these goals, with the capability to characterize rock targets, their submillimetre-scale textural attributes, and potential organic and inorganic biosignatures, placing these features into an outcrop-scale context¹.

Perseverance has explored three geologic terrains in Jezero Crater (Supplementary Fig. 1): (1) the crater floor, which includes lava

flows and igneous cumulates that have experienced aqueous alteration under a variety of conditions^{2,3}; (2) the Western Fan, a sequence of sedimentary rocks derived from mafic to ultramafic sources and deposited in a fluvial-deltaic-lacustrine setting^{4–6}; (3) the Margin Unit, a layered-to-massive sequence of rocks with strong orbital spectroscopic signatures of olivine and carbonate that is exposed between the crater rim and the Western Fan⁷. This study focuses on a suite of rocks exposed in Neretva Vallis, a valley incised through the Jezero Crater rim and Margin Unit, which was the feeder channel for the Western Fan⁸ (Supplementary Fig. 1). Perseverance initially explored a distinct, bright-toned outcrop exposed on the northern margin of Neretva Vallis. This outcrop area is informally named 'Bright Angel' (Fig. 1a). In High Resolution Imaging Science Experiment (HiRISE) images of this

A list of affiliations appears at the end of the paper.

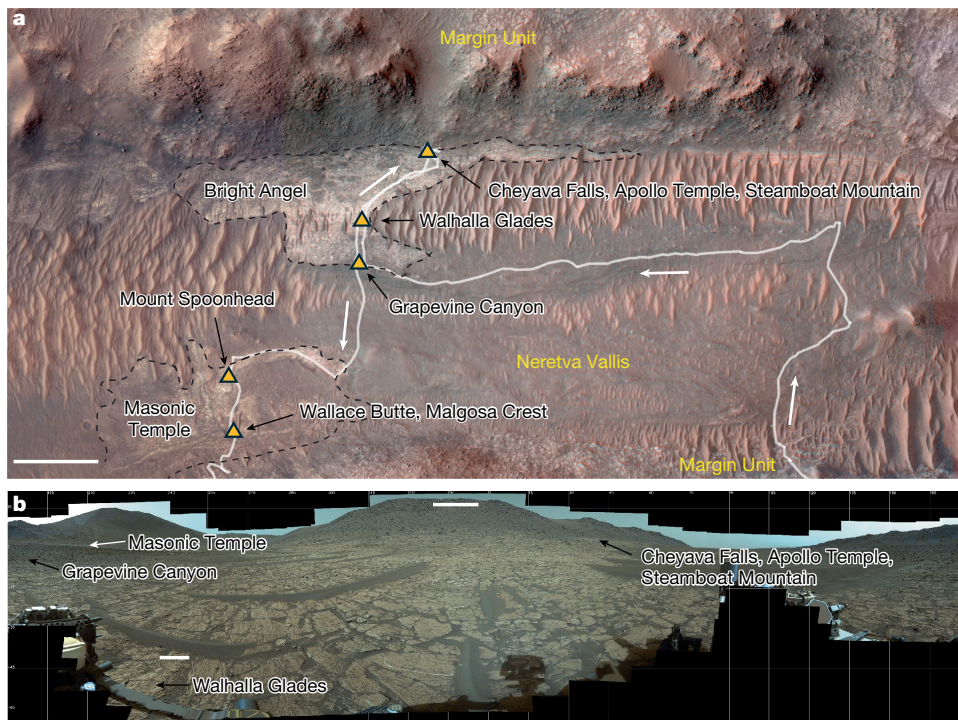


Fig. 1 | Perseverance's path through Neretva Vallis and views of the Bright Angel formation. **a**, Orbital context image with the rover traverse overlain in white. White line and arrows show the direction of the rover traverse from the southern contact between the Margin Unit and Neretva Vallis to the Bright Angel outcrop area and then to the Masonic Temple outcrop area. Labelled orange triangles show the locations of proximity science targets discussed in the text. **b**, Mastcam-Z 360° image mosaic looking at the contact between the light-toned Bright Angel Formation (foreground) and the topographically higher-standing Margin Unit from within the Neretva Vallis channel. This mosaic was collected on sol 1178 from the location of the Walhalla Glades target before

abrasion. Upslope, about 110 m distant, the approximate location of the Beaver Falls workspace (containing the targets Cheyava Falls, Apollo Temple and Steamboat Mountain and the Sapphire Canyon sample) is shown. Downslope, about 50 m distant, the approximate location of the target Grapevine Canyon is also shown. In the distance, at the southern side of Neretva Vallis, the Masonic Temple outcrop area is just visible. Mastcam-Z enhanced colour RGB cylindrical projection mosaic from sol 1178, sequence IDs zcam09219 and zcam09220, acquired at 63-mm focal length. A flyover of this area is available at https://www.youtube.com/watch?v=5FAYABW-c_Q. Scale bars (white), 100 m (**a**), 50 m (**b**, top) and 50 cm (**b**, bottom left). Credit: NASA/JPL-Caltech/ASU/MSSS.

deposit, albedo variations appeared to indicate layering at the metre scale. Subsequently, Perseverance explored strata exposed along the southern margin of Neretva Vallis, in an area informally named 'Masonic Temple' (Fig. 1a), where rocks with similar characteristics crop out. As described below, the outcrops in these areas share many characteristics and are referred to collectively as the Bright Angel formation. Sub-surface structures detected by the Radar Imager for Mars' subsurface experiment (RIMFAX) ground-penetrating radar (GPR; Methods and Supplementary Fig. 2) can be interpreted to indicate that the Bright Angel formation lies stratigraphically above the Margin Unit, but at the present time, we cannot rule out the possibility that the Bright Angel formation represents a part of an older unit.

Outcrop-scale observations

The Bright Angel formation consists of approximately metre-scale blocks formed by fracturing and physical weathering of the exposed outcrop (Fig. 1b). In RIMFAX GPR profiles, radar-reflective layers express a range of apparent dip angles, from horizontal up to about 30° at the northern contact with the Margin Unit (Supplementary Fig. 2). The Bright Angel formation appears to be subdivided into concave-upwards to flat-lying bodies of layered rock lying within the Neretva Vallis channel (Supplementary Fig. 2). Assuming that the observed layer orientations formed during deposition of the Bright Angel formation, the topographically highest-standing outcrops near the contact with the Margin Unit are stratigraphically lower than outcrops farther from the contact.

A representative example of Bright Angel formation outcrop is visible in the 'Beaver Falls' workspace (Fig. 2). Here, the Planetary Instrument

for X-ray Lithochemistry (PIXL), Scanning Habitable Environments with Raman and Luminescence for Organics and Chemicals (SHERLOC) and Wide Angle Topographic Sensor for Operations and Engineering (WATSON), SuperCam, and Mastcam-Z instruments (Methods) analysed a rock containing the targets 'Cheyava Falls' and 'Apollo Temple' and a core sample, named 'Sapphire Canyon', was subsequently collected. In this rock, centimetre-scale, reddish-to-tan-coloured, recessive layers are separated by thinner, relatively resistant, light-toned layers (Figs. 2 and 3a). The layers in this rock dip more steeply and strike at an angle to layers in the nearby outcrop, implying that it may have been displaced from its original orientation. Topographically above but stratigraphically below this rock is a darker-toned rock with a coarsely granular texture, the site of the target 'Steamboat Mountain' (Fig. 2). This darker-toned rock was investigated as a possible transitional lithology between the Bright Angel formation and the Margin Unit.

In general, macroscopic rock textures in the Bright Angel outcrop area are diverse and complex. Intervals of rock are wind-fluted and massive in appearance (Supplementary Fig. 3a), show large (centimetre scale) nodular features (Supplementary Fig. 3b), and are layered and cross-cut by light-toned erosionally resistant and mineralized fractures and veins (Fig. 2 and Supplementary Fig. 3a,b). Primary textures include layered and structureless intervals with limited evidence for transport and deposition by currents, such as cross bedding or plane bed laminations. Across Neretva Vallis, in the Masonic Temple area (Fig. 1a), outcrops express wind-fluted, massive, layered and granular surface textures such as those seen in the Bright Angel area (Supplementary Figs. 4–6). However, the Masonic Temple area also includes poorly sorted conglomerates composed of rounded to subangular

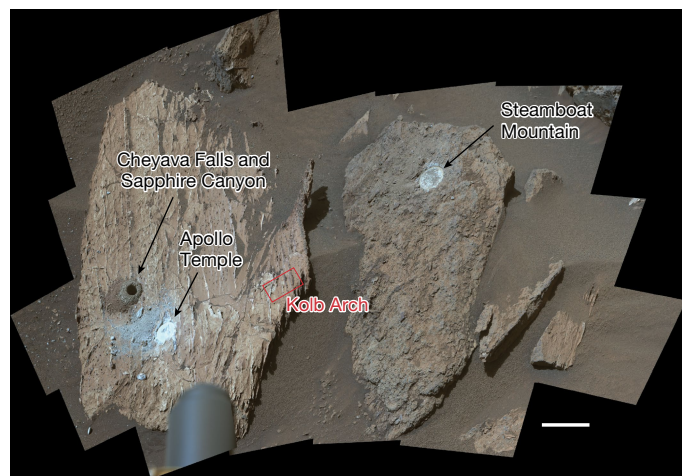


Fig. 2 | The Beaver Falls workspace. Mastcam-Z image mosaic of the Beaver Falls workspace on sol 1217. The light-toned layered block contains the Cheyava Falls natural surface target, the Apollo Temple abrasion and the Sapphire Canyon core sample location. The Sapphire Canyon sample was collected from approximately the same location as Cheyava Falls after analysis of the target was completed. The red box shows the location of the SuperCam target Kolb Arch (Supplementary Fig. 11). The darker-toned granular block contains the Steamboat Mountain abrasion. Downhill is to the left on this image. Mastcam-Z enhanced colour RGB vertical projection mosaic from sol 1217, sequence zcam09264, acquired at 110-mm focal length. Scale bar, 10 cm. Credit: NASA/JPL-Caltech/ASU/MSSS.

millimetre- to centimetre-scale clasts embedded in a fine-grained matrix, as seen in the targets ‘Bass Camp’ (Supplementary Fig. 7) and ‘Wallace Butte’ (Supplementary Fig. 8a,b).

Petrographic relationships

Despite the textural diversity of rocks in the Bright Angel formation, they all contain a fine-grained component, or facies, that comprises much of the rock volume. Individual grains in this facies are not visible in WATSON images (17.9–36.3 μm per pixel) or in SHERLOC Autofocus and Context Imager (ACI) images (10.1 μm per pixel) of the Cheyava Falls target (Fig. 3b,c), indicating grains approximately ≤ 30 –110 μm in diameter, that is, finer than coarse silt or very fine sand. The image resolution is insufficient to determine the relative proportions of clay and silt; accordingly, we classify this facies as mudstone. The Masonic Temple conglomerates contain a matrix made of the same mudstone, as well as abundant millimetre- to centimetre-scale clasts, also composed of mudstone (Supplementary Figs. 7 and 8a,b). These clasts formed by mud deposition, partial consolidation, and later erosion and transport as intraclasts.

The mud facies is red, tan or whitish-grey coloured in different rocks. These colour differences are apparent in visible-light reflectance spectra collected by Mastcam-Z (Supplementary Fig. 9a,b and Supplementary Table 1) and SuperCam (Supplementary Fig. 10 and Supplementary Table 1). Masonic Temple targets are characterized by long-wavelength spectral features that indicate high abundances of ferric iron. This Fe^{3+} imparts strong red colouration. Targets in Bright Angel show spectral features that indicate less Fe^{3+} , resulting in tan to whitish-grey colouration. Near-infrared (NIR) absorption spectra collected by SuperCam (Supplementary Fig. 11a–c) are characterized by shallow, approximately 1.92- μm band depths, indicating that Bright Angel formation rocks are weakly hydrated, especially when compared with sedimentary rocks from the Western Fan (Supplementary Fig. 11d and Supplementary Table 1). Other NIR spectral features are also relatively weak and cannot be uniquely attributed to specific minerals; however, candidate phases include phyllosilicate clays and opaline

silica, consistent with expectations for a mudstone. Calcium sulfate with spectral features consistent with bassanite, $\text{CaSO}_4 \cdot 0.5\text{H}_2\text{O}$, is also identified in NIR spectra (Supplementary Fig. 11e,f).

Organic matter was detected in the Bright Angel area mudstone targets Cheyava Falls, Walhalla Glades and Apollo Temple by the SHERLOC instrument based on the presence of an approximately $1,600\text{-cm}^{-1}$ G band in the Raman spectra^{9–12} (Fig. 3d and Methods). The G band is most intense in Apollo Temple and less intense in Walhalla Glades and Cheyava Falls (Methods). In contrast, no G band was detected at Masonic Temple in the abrasion target ‘Malgosa Crest’. SuperCam Raman spectra collected from Apollo Temple show a strong continuum fluorescence signature (Supplementary Fig. 12) consistent with, but not uniquely attributable to, organic matter; this signature is weak to absent in Malgosa Crest.

PIXL micro-X-ray fluorescence (XRF) elemental analyses indicate that Bright Angel formation mudstone is rich in SiO_2 , Al_2O_3 and FeO , and poor in MgO and MnO (Supplementary Information). On ternary diagrams used to infer mineralogy (Fig. 4a,b), the mudstone plots in locations consistent with abundant silica and aluminosilicate clays. PIXL analysis of the X-ray diffraction properties of the mudstone in abraded patches (Supplementary Fig. 13a–d) shows that it contains only randomly distributed, low-intensity diffraction peaks with no large domains that exhibit coherent monocrystalline diffraction^{13–15}. These properties indicate crystalline domain sizes at or near the PIXL diffraction detection limit of 40–60 μm (ref. 15), in accord with image-based grain size estimates. There is no variation in the crystallinity or textural properties of the mudstone with stratigraphic position or elevation (Supplementary Fig. 13a–d), and thus no evidence for contact metamorphic recrystallization in proximity to adjacent geologic units. Analysis of diffraction peaks detected in calcium-sulfate veins and nodules in three abrasion targets indicates that Ca-sulfate is predominantly non-diffracting as well (Supplementary Figs. 14a–j and 15a–c). Where diffraction was detected and peaks could be indexed¹³ (Methods and Supplementary Table 2), gypsum and anhydrite were identified in isolated small domains. A possible explanation for the high proportion of non-diffracting Ca-sulfate is that it represents fine-grained bassanite, consistent with SuperCam spectra (Supplementary Fig. 11e,f). On Mars, bassanite is known to form by dehydration of gypsum¹⁶, with gypsum precipitation implying low temperature and salinity for Ca-sulfate-precipitating fluids¹⁷.

Finally, olivine sand grains and particulate and intragranular Fe–Mg carbonate were observed in Cheyava Falls and Steamboat Mountain. In Cheyava Falls, PIXL analysed an approximately 0.5–1-mm-diameter olivine grain in an approximately centimetre-thick, light-toned Ca-sulfate layer (Fig. 3a,b). In Steamboat Mountain, coarse to very coarse sand-sized grains (0.5–2 mm) of olivine and Fe–Mg carbonate are locally surrounded by Ca-sulfate and set within mudstone (Supplementary Fig. 13a–h). Mixing relationships between mudstone, olivine, carbonate and Ca-sulfate are illustrated on Fig. 4a,b. Where coarse-crystalline olivine grains and mudstone are in contact with each other (Supplementary Fig. 13b,f), there is no indication that the mudstone has been recrystallized by interaction with this igneous mineral, indicating that olivine is a detrital phase. In Steamboat Mountain, SHERLOC targeted an area containing olivine, carbonate and Ca-sulfate, rather than mudstone. No organic matter was detected, indicating that these phases are not important carriers of organic matter. SuperCam Raman spectra from the Steamboat Mountain mudstone, however, do show the same continuum fluorescence seen in the organic-matter-bearing Apollo Temple target (Supplementary Fig. 12).

Provenance and depositional environments

Observations of the Bright Angel outcrop area are consistent with their interpretation as mudstones deposited from suspension as layered and massive beds. Major element systematics and spectroscopic

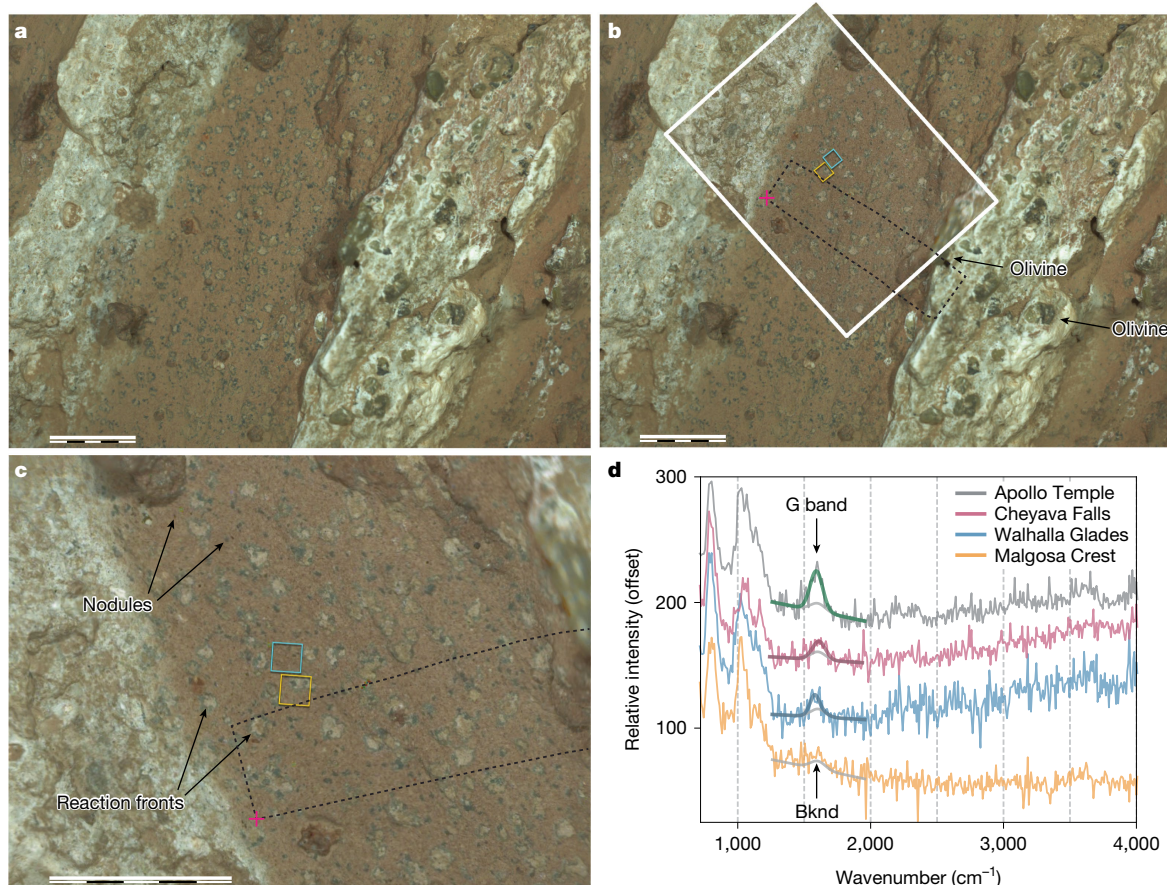


Fig. 3 | Layering, nodules, reaction fronts and organic detections.

a, WATSON nighttime image of Cheyava Falls with both white-light LED groups on acquired on sol 1188 at a stand-off distance of 3.91 cm. Image resolution: $21.0 \pm 0.4 \mu\text{m}$ per pixel. **b**, Colourized SHERLOC ACI image acquired on sols 1201–1202 outlined with a white box and overlain on the WATSON image from **a**. The ACI image is a focus merge of 13 ACI images acquired between stand-off distances of 4.035 cm and 4.335 cm and has an image resolution of about $10 \mu\text{m}$ per pixel. Three $1 \times 1 \text{ mm}$ SHERLOC spectral scans were acquired at the orange square location at stand-off distances of 4.01 cm, 4.035 cm and 4.06 cm. One $1 \times 1 \text{ mm}$ spectral scan was acquired at the blue square location at a stand-off distance of 4.035 cm. The black dotted rectangle shows the footprint of the

PIXL scan acquired from this target. The magenta cross at the corner of the scan provides a reference point for comparison with **c**, which is the colourized SHERLOC ACI image from **b**. The image shows the authigenic nodule and reaction front features as well as the SHERLOC and PIXL scan locations. **d**, SHERLOC Raman spectra from representative targets in the Bright Angel unit with fits to an instrument $-\text{O}-$ stretching overtone feature from the SHERLOC fused-silica optics (light grey, labelled 'Bknd') and the G-band signal at about $1,600 \text{ cm}^{-1}$ associated with organic carbon in the targets Walhalla Glades (blue), Cheyava Falls (red) and Apollo Temple (green fit on grey spectrum). Malgosa Crest (yellow) shows no G-band signal above the instrument background. Scale bars, 5 mm. Credit: NASA/JPL-Caltech/MSSS.

properties indicate that the mudstone provenance was chemically weathered and oxidized, resulting in Si, Al and Fe^{3+} enrichment and Mg and Mn depletion¹⁸. These characteristics are unlike those observed in Western Fan sedimentary rocks, which show little to no fractionation of Fe from Mg or Mn (Supplementary Fig. 16), indicating that they were formed under anoxic conditions¹⁸. At the contact with the Margin Unit (Fig. 2), we observe interstratified bedsets containing both fine-grained mudstone and coarse-grained olivine-bearing layers (for example, Cheyava Falls). We also observe poorly sorted, mud-rich olivine- and carbonate-bearing lithologies (for example, Steamboat Mountain). These coarser-grained lithologies appear to have provided a higher permeability medium through which later Ca-sulfate-precipitating fluids could migrate. Given the olivine- and carbonate-rich nature of the Margin Unit⁷, reworking of grains derived from the Margin Unit into the Bright Angel formation seems plausible. Across Neretva Vallis, at Masonic Temple, the poorly sorted, coarse conglomeratic nature of some outcrops (Supplementary Figs. 7 and 8a,b), and the fine-grained, mud-rich nature of others (Supplementary Fig. 6), indicate significant local or temporal variation in current velocities. Accordingly, we interpret the Bright Angel formation to have formed from sedimentary processes that included weathering, erosion, transport and deposition

from water by fallout from suspension and energetic currents or debris flows, forming mudstone and coarser-grained and conglomeratic lithologies, respectively.

Nodules and reaction fronts

Dispersed throughout the fine-grained mudstone in the Bright Angel outcrop area, we observe approximately $100\text{--}200 \mu\text{m}$ circular to irregularly shaped masses (informally referred to as 'poppy seeds' by the Mars 2020 Science Team) that are black to dark blue to dark green coloured in daytime and nighttime white light-emitting diode (LED) illumination (Fig. 3a–c and Supplementary Figs. 17a,b–19a,b). WATSON (Supplementary Figs. 17c–19c) and PIXL Micro Context Camera (MCC; Supplementary Fig. 20) decorrelation stretch images enhance the blue to green colour of these features relative to the mudstone they occur in. PIXL XRF data indicate that the masses are enriched in Fe, P and Zn relative to their host mudstone (Fig. 4c and Supplementary Fig. 21a–g). On a ternary diagram of FeO-P-CaO (Fig. 4c), they extrapolate towards a molar FeO:P ratio of about 3:2 (see also Supplementary Fig. 21f). The X-ray diffraction properties of these masses are indistinguishable from the surrounding mudstone, indicating crystallites

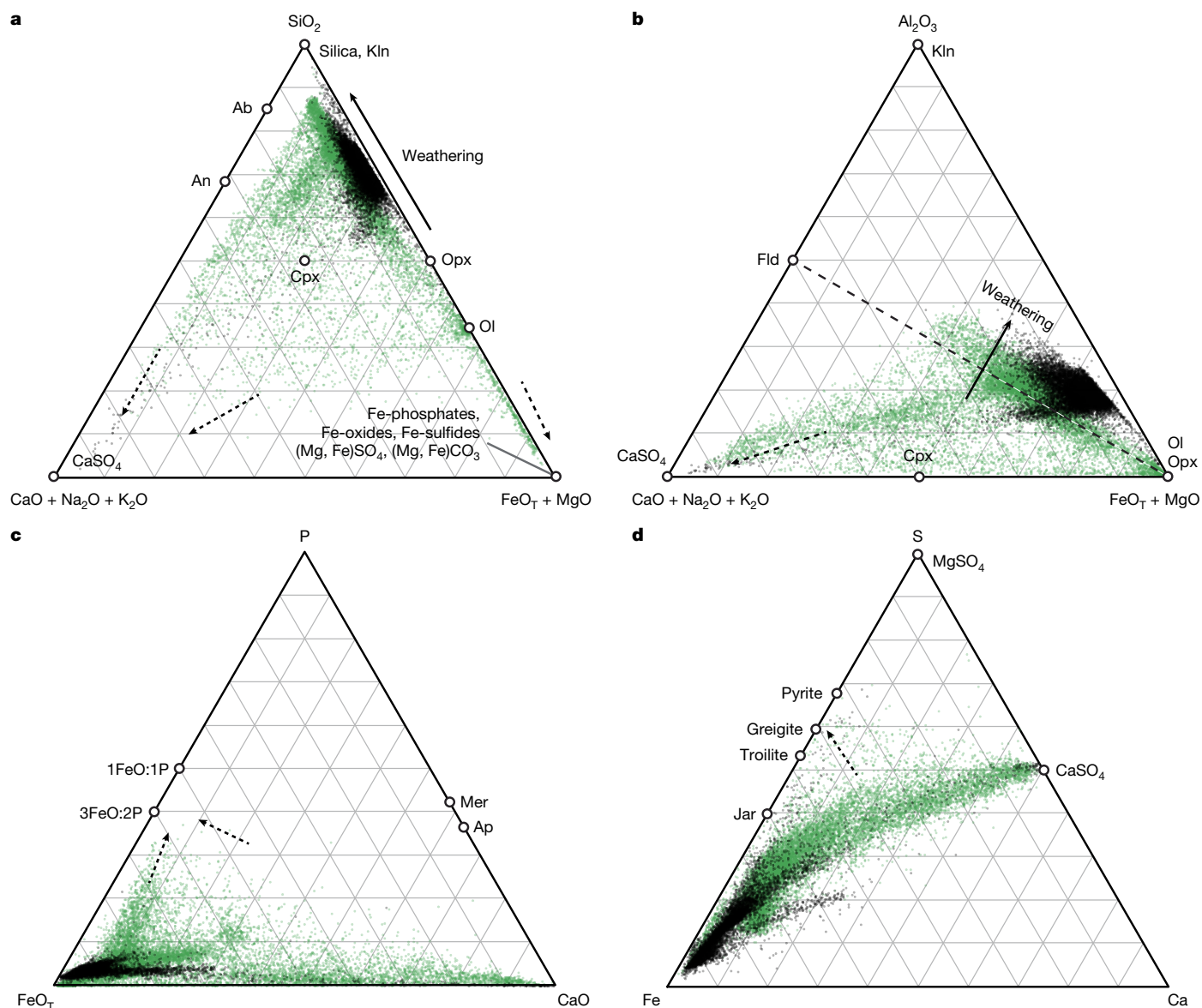


Fig. 4 | Elemental relationships in Bright Angel and Masonic Temple from PIXL. Ternary diagrams plotting molar proportions of the indicated oxides and elements. FeO_T is total iron reported as FeO. Green points are all XRF analyses from the Bright Angel area and black points are from the Masonic Temple area. **a, b**, Complementary diagrams that plot SiO₂ (**a**) and Al₂O₃ (**b**) at their apices. Expected trajectories for oxidative chemical weathering of igneous rocks shown as black arrows; most data points cluster in locations on the diagrams expected for sediments rich in SiO₂, Al₂O₃ and FeO_T, formed by weathering of their sources. In **a**, the cluster of green points near olivine (Ol) represents olivine grains in Steamboat Mountain and Cheyava Falls. Additional linear trends shown with dashed arrowheaded lines indicate mixing with Ca-sulfate (CaSO₄) and Fe-rich phases that include Fe-phosphates, Fe-oxides,

Fe-sulfides, (Mg, Fe)SO₄ and (Mg, Fe)CO₃. Kln, kaolinite; Opx, orthopyroxene; Cpx, clinopyroxene; An, anorthite; Ab, albite; Fld, all feldspars. **c**, Compositional arrays in Bright Angel indicate that an iron-phosphate with a molar 3FeO:2P ratio (stoichiometrically like vivianite, Fe₃(PO₄)₂·8H₂O and its oxidation products) is the primary P-bearing phase. The location of 1FeO:1P ferric phosphate (typically strengite, FePO₄·2H₂O) is also shown. Ap, apatite; Mer, merrillite. **d**, Compositional arrays in Bright Angel and Masonic Temple indicate the presence of CaSO₄. In Bright Angel, an endmember with a molar 3Fe:4S ratio (stoichiometrically like greigite, Fe₃S₄) is also present. Pyrite (FeS₂), troilite (FeS) and jarosite (Jar; KFe³⁺₃(SO₄)₂(OH)₆) are also plotted. The location of the Fe-sulfide minerals on **d** is based on calculations described in Methods.

smaller than 40–60 μm (Supplementary Fig. 13a–d). In the Apollo Temple abrasion, PIXL analyses also reveal abundant Fe-phosphate masses. The colour properties of some of the Fe-phosphate masses in this target are distinctive: colourless in daytime WATSON images, tan/orange-toned under nighttime white-light LED illumination, and red in decorrelation stretch images relative to the surrounding white–grey mud (Supplementary Fig. 22a–c). Combined, these properties are consistent with accumulations of microcrystalline vivianite (Fe²⁺₃(PO₄)₂·8H₂O) or lower-hydration-state ferrous phosphates (for example, phosphoferrite: Fe²⁺₃(PO₄)₂·3H₂O) and their oxidation

products, for example, metavivianite (Fe²⁺_{2.5}Fe³⁺_{0.5}(PO₄)₂·7.5H₂O), ferrostrunzite (Fe²⁺Fe³⁺₂(PO₄)₂(OH)₂·6H₂O) and santabarbaraite (Fe³⁺₃(PO₄)₂(OH)₃·5H₂O), all of which have molar FeO:P ratios of 3:2 and colour properties that match our observations in Bright Angel.

The Fe-phosphate masses do not appear to have been sorted into laminations or lenses of relative enrichment, as might be expected for 100–200 μm accumulations of vivianite co-deposited with finer-grained aluminosilicates and silica. They are thus unlikely to have been transported and deposited as grains along with the surrounding muddy sediment. Instead, the distribution of the Fe-phosphate

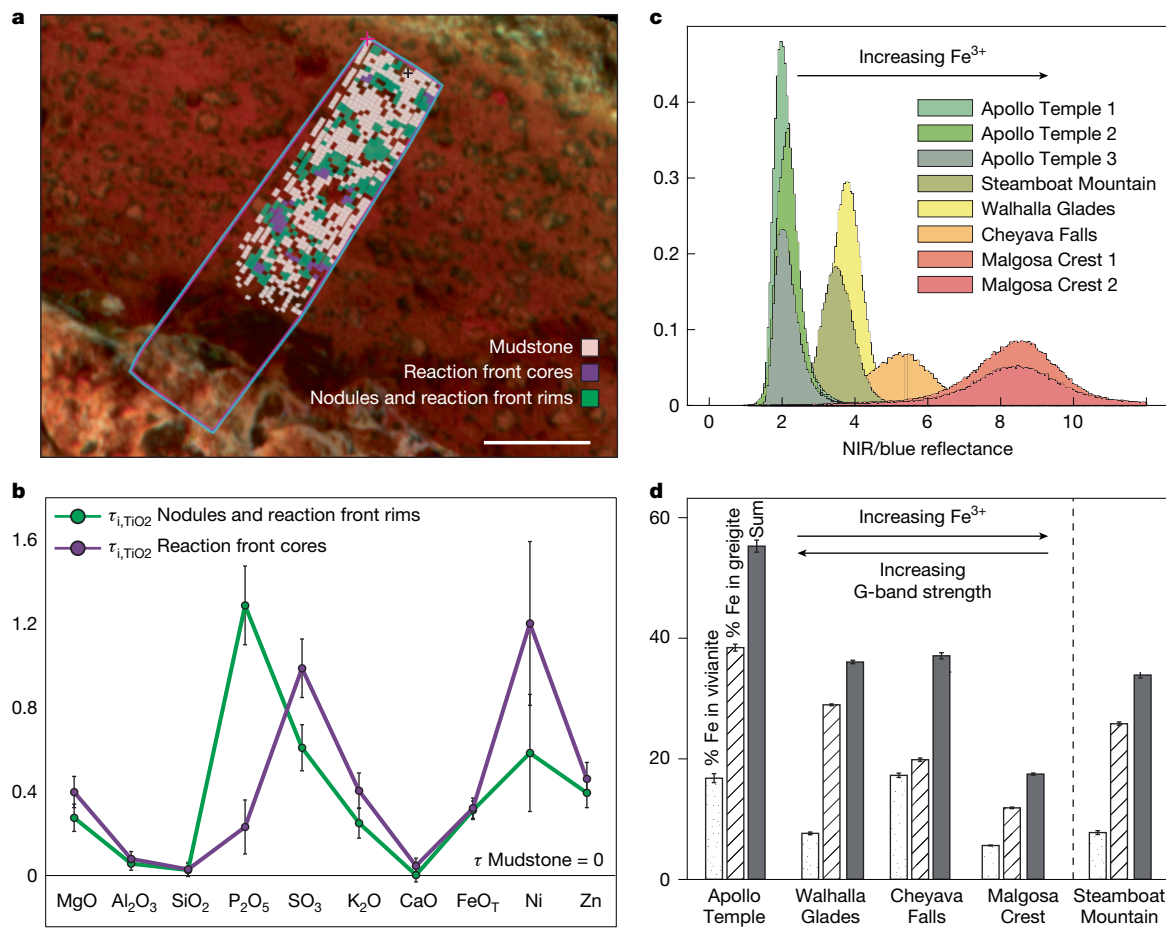


Fig. 5 | Redox processes in Bright Angel and Masonic Temple. a, PIXL MCC colour image of the target Cheyava Falls showing the outline of the PIXL scan area, and the individual XRF analysis points summed together to determine the bulk chemical composition (Supplementary Tables 1–3) of mudstone (tan), reaction front cores (purple), and nodule and reaction front rims (green). Scale bar, 3 mm. **b**, Element mobility index (τ_{i, TiO_2} ; Methods) for the indicated elements in Cheyava Falls showing enrichment and depletion patterns for nodules and reaction front rims (green) and reaction front cores (purple) relative to the mudstone they are contained in. **c**, Normalized probability density function for the NIR/blue reflectance value of individual pixels in PIXL MCC images of the mudstone facies in each of the indicated targets. A higher NIR/blue ratio is associated with higher Fe^{3+} concentration, consistent with a

more oxidized substrate (and vice versa). **d**, Maximum percentage of the total iron in each of the indicated targets that could be present as vivianite (bars with stippled fill), greigite (bars with diagonal line fill) and their sum (grey bars); calculations described in Methods. The Apollo Temple target has the highest calculated vivianite + greigite abundance, the strongest Raman G band (Fig. 3d) and is the least-red target of the group (Fig. 5c). Malgosa Crest has the lowest calculated vivianite + greigite abundance, organic matter is not detected in this target and it is the reddest target of the group (Fig. 5c). Walhalla Glades and Cheyava Falls fall between these two extremes. Steamboat Mountain is separated from the group owing to the lack of constraints on the presence of organic matter in the mudstone in this target. Error bars in **b** and **d** represent propagated standard errors.

masses indicates they formed as the result of chemical processes after mudstone deposition and accordingly can be considered authigenic nodules. In the proximity targets ‘Grapevine Canyon’ and Walhalla Glades, Fe-phosphate nodules are encased in larger, centimetre-scale Ca-sulfate nodules (Supplementary Figs. 13h and 20), which are themselves cross-cut by a later generation of light-toned, mineralized fractures (Supplementary Fig. 3b). Fe-phosphate nodule abundances and sizes seem unrelated to their proximity to either generation of Ca-sulfate, indicating that Ca-sulfate nodule and vein emplacement occurred after Fe-phosphate nodule formation. Fe-phosphate is rare in Masonic Temple area targets. A few isolated spots that might contain Fe-phosphate masses were detected by PIXL in the Malgosa Crest abrasion target and WATSON images showed a few large (about 1–5 mm) blue–green masses (Supplementary Fig. 23a–c), but they were not analysed. These could be authigenic nodules of a different scale or transported Fe-phosphate-enriched clasts.

A striking feature observed in the Cheyava Falls target (and the corresponding Sapphire Canyon core sample), is distinct spots (informally referred to as ‘leopard spots’ by the Mars 2020 Science Team)

that have circular to crenulated dark-toned rims and lighter-toned cores (Fig. 3a–c). The spots range in size from about 200 μm to 1 mm in diameter and their cores are less red than their surrounding mudstone. Like the previously described authigenic nodules they co-occur with, the spots are not concentrated in layers or laminae; together with their irregular shapes, this indicates that they were not deposited as grains. Instead, these multi-coloured features appear to represent in situ reaction fronts.

PIXL XRF analyses of reaction front rims reveal they are enriched in Fe, P and Zn relative to the mudstone they occur in (Fig. 5a,b); we interpret the rims to be made of the same Fe-phosphate minerals found in authigenic nodules. In the reaction front cores, a phase enriched in S, Fe, Ni and Zn was detected (Fig. 5a,b). Insight into the identity of this phase comes from comparison with PIXL analyses of the Apollo Temple target in the same outcrop block as Cheyava Falls (Fig. 2). A ternary diagram of the molar proportions of Fe, S and Ca (Fig. 4d) shows that several spot analyses trend towards a composition on the Fe–S join with an Fe:S ratio of about 3:4. Most of these points are associated with a non-diffracting, millimetre-scale region in the

sol 1213 Apollo Temple XRF map shown in Supplementary Fig. 13c,g. This region, like the reaction front cores, is also enriched in Zn and Ni, approaching values as high as $2,300 \pm 670$ ppm and $2,000 \pm 570$ ppm, respectively (Supplementary Information). We also detect copper in this region at a concentration of 419 ± 355 ppm (Supplementary Information). X-ray scattering properties indicate that both this region and the reaction front cores are light-element-deficient relative to FeO and SO₃ (Supplementary Fig. 24). In LED-illuminated colour images, the high Fe–S region of Apollo Temple contains small dull brown-to-black-coloured masses (Supplementary Fig. 25). Taken together, these chemical and colour properties are consistent with the Fe-sulfide mineral greigite (Fe³⁺₂Fe²⁺S₄; also see Supplementary Fig. 26). The sulfide-bearing region is adjacent to other submillimetre-scale mineral accumulations having properties consistent with Fe and S in a range of oxidation states, including jarosite [KFe³⁺₂(SO₄)₃(OH)₆], which is an oxidation product of Fe-sulfide¹⁹, and a red–brown Fe-rich phase with low SO₃, SiO₂, Al₂O₃ and analytical totals, consistent with siderite (Supplementary Figs. 13g and 25).

Finally, in the Bright Angel formation mudstone facies, there is an inverse relationship between the inferred abundances of vivianite and greigite (Methods and Supplementary Information) versus mudstone oxidation state, inferred from the NIR/blue reflectance ratio in PIXL MCC images²⁰. The NIR/blue ratio is sensitive to the relative abundance of Fe³⁺, like observations from Mastcam-Z (Supplementary Fig. 9a,b) and SuperCam (Supplementary Fig. 10). This inverse relationship is shown in Fig. 5c,d. Mudstone oxidation state also appears to be inversely related to the strength of the SHERLOC Raman G band. As shown in Fig. 5c,d, the Apollo Temple mudstone has the strongest G band, the highest inferred vivianite + greigite abundance, and the least-oxidized colour properties. In contrast, Malgosa Crest has no detectable organic matter, the lowest inferred vivianite + greigite abundance, and is the most-oxidized target analysed in the Bright Angel formation. Walhalla Glades and Cheyava Falls are intermediate between these two extremes.

An exploration of reaction mechanisms

Chemical and sedimentological data indicate that reduced iron and sulfur were generated, mobilized and precipitated following the deposition of fine-grained oxidized iron- and phosphorous-bearing sediment. Except when found in authigenic nodules and reaction front rims, phosphate is not associated with a mineral phase (for example, there is no indication that apatite or merrillite are present; Fig. 4c). Accordingly, we suggest that during deposition, phosphate was adsorbed on Fe³⁺, Al- and Si-rich sediment grains²¹. In the Bright Angel area, iron and phosphate have been redistributed into authigenic nodules and reaction front rims; mass balance calculations suggest closed-system reorganization of these chemical components into vivianite (Supplementary Text). Fe-phosphate-enriched masses are not associated with Al₂O₃ (Supplementary Fig. 21h), which might otherwise suggest the co-existence of Al-phosphate minerals typical of transport of Al³⁺ and Fe³⁺ under oxidizing, low-pH conditions, such as variscite (AlPO₄·2H₂O) and strengite (FePO₄·2H₂O)^{22,23} (Fig. 4c). Instead, transport of Fe²⁺, Zn²⁺ and PO₄³⁻ probably occurred under non-oxidizing conditions, which, combined with moderate pH, prevented mobilization of Al³⁺. Such conditions favour the precipitation of vivianite²³. The apparent absence of Fe-phosphate nodules and reaction fronts in most of the conglomerate-bearing Masonic Temple area suggests a depositional facies control on the development of these specific features.

In the Bright Angel area, Fe-phosphate minerals are associated with organic matter (Fig. 3d). A pathway to the formation of vivianite is via the oxidation of this organic matter, which would have been coupled to the reductive dissolution of Fe³⁺ in sediment grains. This process would have liberated Fe²⁺ and PO₄³⁻ to solution and precipitated Fe²⁺-phosphate. Similar precipitation and redox reactions have been

considered for an occurrence of Mn–P-rich nodules in Gale Crater²⁴, and for submillimetre-scale mixed valence Fe-phosphate grains in a conglomerate outcrop in the Jezero Western Fan^{25,26}. Sulfate reduction coupled to organic matter oxidation could also be responsible for precipitation of Fe-sulfide in the Apollo Temple target and in the cores of reaction fronts in Cheyava Falls. As reduced Fe- and S-bearing phases formed, the mudstone colour properties were modified by iron reduction, bleaching it of its red colour in proportion to the abundance of available organic matter (Fig. 5c,d).

Here we consider the null hypothesis: that within the low-temperature sedimentary-diagenetic setting we have proposed for the Bright Angel formation, abiotic reactions produced ferrous Fe and reduced S and concentrated them in authigenic nodules and reaction fronts. The null hypothesis predicts that abiotic reactions can reduce sedimentary Fe³⁺ to aqueous Fe²⁺, which is then incorporated in the Fe-phosphate and Fe-sulfide minerals we have identified. A wide variety of organic carbon compounds are known to promote the abiotic reductive dissolution of ferric iron oxide minerals at temperatures between 10 °C and 80 °C (refs. 27–29). The presence of organic matter in Bright Angel formation mudstone (Fig. 3d), which could have been produced on Mars through abiotic synthesis^{30,31} or delivered from non-biological exogenic sources^{30,32}, suggests that such reactions could have occurred. Further analysis is required to determine whether the specific organic compounds present in the Bright Angel formation can drive the reduction of mineral-hosted sedimentary Fe³⁺ at low temperature. Another possible pathway to the production of Fe²⁺ is through the abiotic oxidation of pyrite by Fe³⁺ (aq)³³. This process would require both the presence of detrital pyrite and low solution pH, which would permit Fe³⁺ (aq) to be present. As previously discussed, neither condition appears to be met in the Bright Angel formation.

The null hypothesis also predicts that an abiotic source of dissolved sulfide was available to be incorporated in authigenic Fe-sulfide. Dissolved sulfide facilitates the reductive dissolution of ferric iron oxides, with half-lives ranging from years to hours depending on Fe-oxide mineralogy, crystallinity and pH^{34,35}, providing another potential pathway to the production of Fe²⁺ (aq). Magmatic degassing of reduced sulfur-bearing gases (for example, ref. 36) to local groundwater could provide a potential source of dissolved sulfide during diagenesis. However, geological constraints demand that this sulfide migrate in from a distal, high-temperature sulfide-gas-producing system, to the low-temperature depositional-diagenetic environment of the Bright Angel formation. No evidence for sulfide-producing hydrothermal or magmatic systems was observed in the Crater Floor, Western Fan or Margin Unit before investigation of the Bright Angel formation. Abiotic reduction of sulfate to sulfide by organic matter is another possible source of dissolved sulfide that could both reduce Fe³⁺-bearing sediment and provide the reduced sulfur required to form Fe-sulfide minerals³⁷. However, sulfate reduction by reduced carbon compounds is energetically demanding and kinetically inhibited by the symmetry of the SO₄²⁻ ion³⁸, so abiotic reaction rates are exceedingly slow at temperatures <150–200 °C (refs. 37,38). As discussed previously, the Bright Angel formation shows no unambiguous evidence that it was heated in contact with adjacent geologic units, and burial to depths in excess of about 5 km would be required to achieve temperatures >150 °C during the Noachian³⁹.

Given the potential challenges to the null hypothesis, we consider here an alternative biological pathway for the formation of authigenic nodules and reaction fronts. On Earth, vivianite nodules are known to form in fresh water^{23,40,41} and marine^{42,43} settings as a by-product of low-temperature microbially mediated Fe-reduction reactions. Fe-sulfide minerals, such as greigite, pyrite and mackinawite, can also be formed as products of microbial sulfate reduction^{44,45}, and have been observed in close spatial association with vivianite⁴². Greigite precipitation, from precursor mackinawite, is favoured by a high dissolved Fe²⁺/SO₄²⁻ ratio, typical of diagenetic fluids in freshwater and

ferruginous marine environments⁴⁴. Repeated sulfidation of Fe²⁺ in vivianite followed by sulfide oxidation promotes stable incorporation of Zn and other heavy metals into vivianite⁴⁶. Thus, Zn enrichment in nodules is consistent with a hybrid iron- and sulfate-reducing mechanism. Minerals like these, produced by Fe- and S-based metabolisms, provide some of the earliest chemical evidence for life on Earth^{47,48}, and are thought to represent potential biosignatures in the search for life on Mars⁴⁹. The fact that the reaction fronts observed in the Cheyava Falls target are defined by small, spot-shaped, bleached zones in an overall Fe-oxide-bearing, red-coloured rock invites comparison to terrestrial ‘reduction halos’ in modern marine sediments⁵⁰ and ‘reduction spots’, which are concentrically zoned features found in rocks of Precambrian and younger age on Earth⁵¹. A biologically influenced origin has been proposed by some for reduction spots⁵¹, although this is not a universally held perspective⁵².

Under a biological scenario, the mixture of reactants available in the Bright Angel formation at the time of deposition could have provided raw ingredients for a set of biological redox reactions that drove Fe and S reduction, organic matter oxidation, and precipitation of Fe²⁺-phosphate and Fe-sulfide minerals. In this scenario, oxidized iron and sulfate would be used as terminal electron acceptors for organic matter consumption, promoting the formation of minerals through the release of chemical by-products: Fe-phosphate minerals in the case of iron reduction and Fe-sulfide minerals in the case of sulfate reduction. Where authigenic nodules were formed, the reaction would have shut off before additional reductive processes occurred. In the places where larger reaction fronts formed, the presence of sulfide-bearing cores suggests that sulfate-reducing metabolisms with lower energy yields could have taken hold once those regions of the rock had been depleted of available Fe³⁺, but had not yet exhausted organic carbon in the reaction front core.

In summary, our analysis leads us to conclude that the Bright Angel formation contains textures, chemical and mineral characteristics, and organic signatures that warrant consideration as ‘potential biosignatures’^{53–55}, that is, “a feature that is consistent with biological processes and that, when encountered, challenges the researcher to attribute it either to inanimate or to biological processes, compelling them to gather more data before reaching a conclusion as to the presence or absence of life”⁵³. This assessment is further supported by the geological context of the Bright Angel formation, which indicates that it is sedimentary in origin and deposited from water under habitable conditions. Many significant questions remain about the origin of the nodules and reaction fronts encountered by Perseverance. We suggest that further in situ, laboratory, modelling and field analogue research into both abiotic and biological processes that give rise to the suite of mineral and organic phases observed in the Bright Angel formation will improve our understanding of the conditions under which they formed. Ultimately, the return of samples from Mars for study on Earth, including the Sapphire Canyon sample collected from the Bright Angel formation, would provide the best opportunity to understand the processes that gave rise to the unique features described here.

Online content

Any methods, additional references, Nature Portfolio reporting summaries, source data, extended data, supplementary information, acknowledgements, peer review information; details of author contributions and competing interests; and statements of data and code availability are available at <https://doi.org/10.1038/s41586-025-09413-0>.

1. Farley, K. A. et al. Mars 2020 mission overview. *Space Sci. Rev.* <https://doi.org/10.1007/s11214-020-00762-y> (2020).
2. Farley, K. A. et al. Aqueously altered igneous rocks sampled on the floor of Jezero Crater, Mars. *Science* **377**, eabo2196 (2022).
3. Simon, J. I. et al. Samples collected from the floor of Jezero Crater with the Mars 2020 Perseverance rover. *J. Geophys. Res. Planets* <https://doi.org/10.1029/2022JE007474> (2023).

4. Mangold, N. et al. Perseverance rover reveals an ancient delta-lake system and flood deposits at Jezero Crater, Mars. *Science* **374**, 711–717 (2021).
5. Stack, K. M. et al. Sedimentology and stratigraphy of the Shenandoah Formation, Western Fan, Jezero Crater, Mars. *J. Geophys. Res. Planets* <https://doi.org/10.1029/2023JE008187> (2024).
6. Bosak, T. et al. Astrobiological potential of rocks acquired by the Perseverance rover at a sedimentary fan front in Jezero Crater, Mars. *AGU Adv.* <https://doi.org/10.1029/2024AV001241> (2024).
7. Horgan, B. H. N., Anderson, R. B., Dromart, G., Amador, E. S. & Rice, M. S. The mineral diversity of Jezero Crater: evidence for possible lacustrine carbonates on Mars. *Icarus* <https://doi.org/10.1016/j.icarus.2019.113526> (2020).
8. Goudge, T. A., Mustard, J. F., Head, J. W., Fassett, C. I. & Wiseman, S. M. Assessing the mineralogy of the watershed and fan deposits of the Jezero Crater paleolake system, Mars. *J. Geophys. Res. Planets* **120**, 775–808 (2015).
9. Steele, A. et al. Comprehensive imaging and Raman spectroscopy of carbonate globules from Martian meteorite ALH 84001 and a terrestrial analogue from Svalbard. *Meteorit. Planet. Sci.* **42**, 1549–1566 (2007).
10. Steele, A. et al. Macromolecular carbon in Martian basalts. *Meteorit. Planet. Sci.* **47**, A357–A357 (2012).
11. Bhartia, R. et al. Perseverance’s Scanning Habitable Environments with Raman and Luminescence for Organics and Chemicals (SHERLOC) investigation. *Space Sci. Rev.* **217**, 58 (2021).
12. Scheller, E. L. et al. Inorganic interpretation of luminescent materials encountered by the Perseverance rover on Mars. *Sci. Adv.* **10**, eadm8241 (2024).
13. Jones, M. W. M. et al. In situ crystallographic mapping constrains sulfate precipitation and timing in Jezero Crater, Mars. *Sci. Adv.* **11**, eadt3048 (2025).
14. Orenstein, B. J. et al. In-situ mapping of monocrystalline regions on Mars. *Icarus* **420**, 116202 (2024).
15. Tice, M. M. et al. Alteration history of Seitha Formation rocks inferred by PIXL X-ray fluorescence, X-ray diffraction, and multispectral imaging on Mars. *Sci. Adv.* **8**, eabp9084 (2022).
16. Vaniman, D. T. et al. Gypsum, bassanite, and anhydrite at Gale Crater, Mars. *Am. Mineral.* **103**, 1011–1020 (2018).
17. Hardie, L. A. Gypsum-anhydrite equilibrium at one atmosphere pressure. *Am. Mineral.* **52**, 171–17 (1967).
18. Babechuk, M. G., Widdowson, M. & Kamber, B. S. Quantifying chemical weathering intensity and trace element release from two contrasting basalt profiles, Deccan Traps, India. *Chem. Geol.* **363**, 56–75 (2014).
19. Burns, R. G. & Fisher, D. S. Iron–sulfur mineralogy of Mars—magmatic evolution and chemical-weathering products. *J. Geophys. Res. Solid Earth* **95**, 14415–14421 (1990).
20. Henneke, J. et al. A radiometric correction method and performance characteristics for PIXL’s multispectral analysis using LEDs. *Space Sci. Rev.* <https://doi.org/10.1007/s11214-023-01014-5> (2023).
21. Rampe, E. B., Morris, R. V., Archer, P. D., Agresti, D. G. & Ming, D. W. Recognizing sulfate and phosphate complexes chemisorbed onto nanopase weathering products on Mars using in-situ and remote observations. *Am. Mineral.* **101**, 678–689 (2016).
22. Roncal-Herrero, T., Rodríguez-Blanco, J. D., Benning, L. G. & Oelkers, E. H. Precipitation of iron and aluminum phosphates directly from aqueous solution as a function of temperature from 50 to 200°C. *Crys. Growth Des.* **9**, 5197–5205 (2009).
23. Nriagu, J. & Dell, C. Diagenetic formation of iron phosphates in recent lake sediments. *Am. Mineral.* **59**, 934–946 (1974).
24. Treiman, A. H. et al. Manganese–iron phosphate nodules at the Grotto Site, Gale Crater, Mars. *Minerals* <https://doi.org/10.3390/min13091122> (2023).
25. Hausrath, E. M. et al. Phosphates on Mars and their importance as igneous, aqueous, and astrobiological indicators. *Minerals* <https://doi.org/10.3390/min14060591> (2024).
26. Kizovski, T. et al. Fe-phosphates in Jezero Crater as evidence for an ancient habitable environment on Mars. *Nat. Commun.* **16**, 6470 (2025).
27. Miller, W. P., Zelazny, L. W. & Martens, D. C. Dissolution of synthetic crystalline and noncrystalline iron oxides by organic acids. *Geoderma* **37**, 1–13 (1986).
28. Torres, R., Blesa, M. A. & Matijević, E. Interactions of metal hydrous oxides with chelating agents: IX. Reductive dissolution of hematite and magnetite by aminocarboxylic acids. *J. Colloid Interface Sci.* **134**, 475–485 (1990).
29. Ionescu, D., Heim, C., Polerecky, L., Thiel, V. & De Beer, D. Biotic and abiotic oxidation and reduction of iron at circumneutral pH are inseparable processes under natural conditions. *Geomicrobiol. J.* **32**, 221–230 (2015).
30. Eigenbrode, J. L. et al. Organic matter preserved in 3-billion-year-old mudstones at Gale Crater, Mars. *Science* **360**, 1096–1101 (2018).
31. Steele, A. et al. Organic synthesis associated with serpentinization and carbonation on early Mars. *Science* **375**, 172–177 (2022).
32. Flynn, G. J., Nittler, L. R. & Engrand, C. Composition of cosmic dust: sources and implications for the early Solar System. *Elements* **12**, 177–183 (2016).
33. Rimstidt, J. D. & Vaughan, D. J. Pyrite oxidation: a state-of-the-art assessment of the reaction mechanism. *Geochim. Cosmochim. Acta* **67**, 873–880 (2003).
34. Afonso, M. D. & Stumm, W. Reductive dissolution of iron(III) (hydr)oxides by hydrogen-sulfide. *Langmuir* **8**, 1671–1675 (1992).
35. Canfield, D. E., Raiswell, R. & Bottrell, S. The reactivity of sedimentary iron minerals toward sulfide. *Am. J. Sci.* **292**, 659–683 (1992).
36. Gaillard, F. & Scaillet, B. The sulfur content of volcanic gases on Mars. *Earth Planet. Sci. Lett.* **279**, 34–43 (2009).
37. Machel, H. G. Bacterial and thermochemical sulfate reduction in diagenetic settings—old and new insights. *Sediment. Geol.* **140**, 143–175 (2001).
38. Rickard, D. & Luther, G. W. Chemistry of iron sulfides. *Chem. Rev.* **107**, 514–562 (2007).
39. McSween, H. Y. Jr., Labotka, T. C. & Viviano-Beck, C. E. Metamorphism in the Martian crust. *Meteorit. Planet. Sci.* **50**, 590–603 (2015).
40. Cosmidis, J. et al. Biomineralization of iron-phosphates in the water column of Lake Pavin (Massif Central, France). *Geochim. Cosmochim. Acta* **126**, 78–96 (2014).

41. Vuillemin, A. et al. Vivianite formation in ferruginous sediments from Lake Towuti, Indonesia. *Biogeosciences* **17**, 1955–1973 (2020).
42. Hsu, T. W., Jiang, W. T. & Wang, Y. S. Authigenesis of vivianite as influenced by methane-induced sulfidization in cold-seep sediments off southwestern Taiwan. *J. Asian Earth Sci.* **89**, 88–97 (2014).
43. Liu, J. R. et al. Vivianite formation in methane-rich deep-sea sediments from the South China Sea. *Biogeosciences* **15**, 6329–6348 (2018).
44. Rickard, D., Roberts, A. P. & Navrotsky, A. Sedimentary greigite formation. *Am. J. Sci.* <https://doi.org/10.2475/OOIc.121855> (2024).
45. Picard, A., Gartman, A., Clarke, D. R. & Girguis, P. R. Sulfate-reducing bacteria influence the nucleation and growth of mackinawite and greigite. *Geochim. Cosmochim. Acta* **220**, 367–384 (2018).
46. Xu, Z. Y. et al. Sulfidation-reoxidation enhances heavy metal immobilization by vivianite. *Water Res.* **263**, 122195 (2024).
47. Craddock, P. R. & Dauphas, N. Iron and carbon isotope evidence for microbial iron respiration throughout the Archean. *Earth Planet. Sci. Lett.* **303**, 121–132 (2011).
48. Marin-Carbonne, J. et al. In situ Fe and S isotope analyses in pyrite from the 3.2 Ga Mendon Formation (Barberton Greenstone Belt, South Africa): evidence for early microbial iron reduction. *Geobiology* **18**, 306–325 (2020).
49. Banfield, J. F., Moreau, J. W., Chan, C. S., Welch, S. A. & Little, B. Mineralogical biosignatures and the search for life on Mars. *Astrobiology* **1**, 447–465 (2001).
50. Thomson, J., Higgs, N. C. & Colley, S. A geochemical investigation of reduction haloes developed under turbidities in brown clay. *Mar. Geol.* **89**, 315–330 (1989).
51. Spinks, S. C., Parnell, J. & Bowden, S. A. Reduction spots in the Mesoproterozoic age: implications for life in the early terrestrial record. *Int. J. Astrobiol.* **9**, 209–216 (2010).
52. Kawahara, H. et al. Bleached-spot formation in Fe-oxide-rich rock by inorganic process. *Chem. Geol.* **609**, 121049 (2022).
53. Des Marais, D. J. et al. The NASA astrobiology roadmap. *Astrobiology* **3**, 219–235 (2003).
54. Gillen, C., Jeancolas, C., McMahon, S. & Vickers, P. The call for a new definition of biosignature. *Astrobiology* **23**, 1228–1237 (2023).
55. Mustard, J. F. et al. *Report of the Mars 2020 Science Definition Team* (Mars Exploration Program Analysis Group, 2013).

Publisher's note Springer Nature remains neutral with regard to jurisdictional claims in published maps and institutional affiliations.



Open Access This article is licensed under a Creative Commons Attribution-NonCommercial-NoDerivatives 4.0 International License, which permits any non-commercial use, sharing, distribution and reproduction in any medium or format, as long as you give appropriate credit to the original author(s) and the source, provide a link to the Creative Commons licence, and indicate if you modified the licensed material. You do not have permission under this licence to share adapted material derived from this article or parts of it. The images or other third party material in this article are included in the article's Creative Commons licence, unless indicated otherwise in a credit line to the material. If material is not included in the article's Creative Commons licence and your intended use is not permitted by statutory regulation or exceeds the permitted use, you will need to obtain permission directly from the copyright holder. To view a copy of this licence, visit <http://creativecommons.org/licenses/by-nc-nd/4.0/>.

© The Author(s) 2025

¹Department of Geosciences, Stony Brook University, Stony Brook, NY, USA. ²Department of Geology and Geophysics, Texas A&M University, College Station, TX, USA. ³Jet Propulsion Laboratory, California Institute of Technology, Pasadena, CA, USA. ⁴Planetary Science

Institute, Tucson, AZ, USA. ⁵School of Earth and Space Exploration, Arizona State University, Tempe, AZ, USA. ⁶Department of Earth, Atmospheric and Planetary Sciences, Massachusetts Institute of Technology, Cambridge, MA, USA. ⁷Department of Earth, Atmospheric, and Planetary Sciences, Purdue University, West Lafayette, IN, USA. ⁸Deutsches Zentrum für Luft- und Raumfahrt (DLR), Institute of Optical Sensor Systems, Berlin, Germany. ⁹Institut de Recherche en Astrophysique et Planétologie, CNRS, Univ. Toulouse, CNES, Toulouse, France. ¹⁰Université Claude Bernard Lyon 1, ENS de Lyon, CNRS, UJM, LGL-TPE, UMR 5276, Villeurbanne, France. ¹¹Division of Geological and Planetary Sciences, California Institute of Technology, Pasadena, CA, USA. ¹²Department of Earth Science and Engineering, Imperial College London, London, UK. ¹³Center for Space Sensors and Systems, University of Oslo, Oslo, Norway. ¹⁴School of Natural Sciences, Birkbeck, University of London, London, UK. ¹⁵Johns Hopkins University Applied Physics Laboratory, Laurel, MD, USA. ¹⁶Central Analytical Research Facility, Queensland University of Technology, Brisbane, Queensland, Australia. ¹⁷School of Chemistry and Physics, Queensland University of Technology, Brisbane, Queensland, Australia. ¹⁸Technical University of Denmark, DTU Space, Kongens Lyngby, Denmark. ¹⁹Earth, Environmental and Planetary Sciences, University of Tennessee, Knoxville, TN, USA. ²⁰Department of Earth Sciences, Brock University, St. Catharines, Ontario, Canada. ²¹Astromaterials Research and Exploration Science Division, NASA Johnson Space Center, Houston, TX, USA. ²²Department of Earth, Environmental, and Planetary Sciences, Rice University, Houston, TX, USA. ²³Joanneum Research Institute for Digital Technologies, Graz, Austria. ²⁴Department of Earth, Planetary and Space Sciences, University of California Los Angeles, Los Angeles, CA, USA. ²⁵Malin Space Science Systems, San Diego, CA, USA. ²⁶Geology Department, Western Washington University, Bellingham, WA, USA. ²⁷RISE Research Institutes of Sweden, Stockholm, Sweden. ²⁸Carnegie Science Earth and Planets Laboratory, Washington DC, USA. ²⁹Department of Earth Sciences, University of Cambridge, Cambridge, UK. ³⁰Lunar and Planetary Institute, Houston, TX, USA. ³¹Department of Earth, Environmental, and Planetary Sciences, Washington University in St. Louis, St. Louis, MO, USA. ³²Blue Marble Space Institute of Science, Seattle, USA. ³³Department of Lithospheric Research, University of Vienna, Vienna, Austria. ³⁴Institut d'astrophysique et de planétologie de Grenoble/ISTerre, Grenoble, France. ³⁵IMPMC, UMR 7590 SU, CNRS, MNHN, IRD Biominingology Team Jussieu Campus, Paris, France. ³⁶Museum National d'Histoire Naturelle, CNRS UMR 7590, Sorbonne Université, IMPMC, Paris, France. ³⁷Institut de Minéralogie, de Physique des Matériaux et de Cosmochimie, CNRS UMR 7590, Sorbonne Université, Muséum National d'Histoire Naturelle, Paris, France. ³⁸Photon Systems Inc., Covina, CA, USA. ³⁹Plancius Research, Manlius, NY, USA. ⁴⁰Géosciences Environnement Toulouse, UMR 5563 Université de Toulouse, CNRS, IRD, CNES, Toulouse, France. ⁴¹Centre for Terrestrial and Planetary Exploration, University of Winnipeg, Winnipeg, Manitoba, Canada. ⁴²Centro de Astrobiología (CAB), CSIC-INTA, Madrid, Spain. ⁴³School of Earth and Atmospheric Sciences, Queensland University of Technology, Brisbane, Queensland, Australia. ⁴⁴INAF-Astrophysical Observatory of Arcetri, Florence, Italy. ⁴⁵Observatoire de Paris, PSL, Paris, France. ⁴⁶Department of Geoscience, UNLV, Las Vegas, NV, USA. ⁴⁷Department of Earth and Atmospheric Sciences, University of Alberta, Edmonton, Alberta, Canada. ⁴⁸Department of Earth and Space Sciences/Astrobiology Program, University of Washington, Seattle, WA, USA. ⁴⁹Univ. Grenoble Alpes, CNRS, IPAG, Grenoble, France. ⁵⁰Laboratoire Planétologie et Géosciences, CNRS UMR6112, Nantes Université, Univ. Angers, Nantes, France. ⁵¹ERICA Research Group and LaDIS Laboratory, University of Valladolid, Valladolid, Spain. ⁵²Institute of Geosciences, CSIC-UCM, Madrid, Spain. ⁵³Mars Exploration Program, NASA Headquarters, Washington DC, USA. ⁵⁴Department of Earth and Planetary Science, University of California Berkeley, Berkeley, CA, USA. ⁵⁵Los Alamos National Laboratory, Los Alamos, NM, USA. ⁵⁶e-mail: joel.hurowitz@stonybrook.edu

Methods

Science instruments

The data used in this contribution were produced by: (1) the RIMFAX ground-penetrating radar⁵⁶; (2) PIXL and its associated MCC⁵⁷; (3) the SHERLOC instrument and its associated WATSON and ACI camera systems¹¹; (4) the SuperCam instrument^{58,59}; and (5) the Mastcam-Z instrument⁶⁰.

Rock-surface preparation for analysis

Naturally exposed rock surfaces were prepared by removing surface dust with the gas dust removal tool⁶¹. To observe less weathered or flatter surfaces, several rocks were abraded using the rover's abrading bit⁶¹ to produce circular approximately 5-cm-diameter-wide by approximately 5–10-mm-deep 'abrasion patches'. Target names, surface preparation techniques, unit and outcrop associations, and the images that each target appears in are tabulated in Supplementary Table 3.

SHERLOC measurements

An overview of SHERLOC image and spectral map acquisition and standard processing methods are described in refs. 11,62. Colourized ACI images were produced using methods described in ref. 62. A focus mechanism motor failure on sol 1024 required SHERLOC measurements reported here to rely entirely on positioning by Perseverance's robotic arm, without the capability to refine focus internally. Bright Angel measurements were therefore made at a systematic offset from best focus: sol 1180 Walhalla Glades was collected at approximately 1.2-mm offset, sol 1201 Cheyava Falls was collected at approximately 1.8-mm offset, and sol 1217 Apollo Temple was collected at approximately 1.1-mm offset. Sol 1242 Malgosa Crest was collected at <0.3-mm offset from best focus; the absence of a G-band signal at Malgosa Crest, despite its better placement, provides further confidence in the G-band peak classification of the other Bright Angel spectra. The spectral intensity is attenuated for measurements collected out of focus, with approximately 35% signal loss expected for 1.5-mm focus offsets. No other spectral artefacts are expected for out of focus measurements. The Raman D band, normally associated in visible Raman spectra with disordered carbonaceous matter such as kerogen, is not present in SHERLOC spectra from the Bright Angel targets. The D band is generally less prominent in deep-ultraviolet (for SHERLOC, 248.6 nm) Raman spectra than Raman spectra that rely on visible-light-wavelength excitation sources⁶³. Furthermore, the focus offset associated with measurements collected at Bright Angel is expected to reduce the observed Raman signal of a potential D-band peak to the instrument noise level, as confirmed with focus offset tests on the organic-rich SaU 008 SHERLOC calibration target and with SHERLOC analogue laboratory instruments. The SHERLOC fused-silica window generates a minor optical background contribution that must be accounted for in SHERLOC spectra, as described by ref. 64. The Si–O-stretching overtone feature in the 1,600 cm⁻¹ region is shown in Fig. 3d (grey traces) for comparison with target spectra, demonstrating the significantly larger contribution of the G-band signal to this spectral region for Bright Angel measurements.

PIXL element and mineral abundance estimates

In the Supplementary Data Tables, the bulk chemical composition determined from the sum of all XRF spectra collected by PIXL from each target is provided along with a black-and-white PIXL MCC image showing the footprint of the PIXL XRF scan area on the target. The sol number that the XRF and MCC data were collected on is shown, along with the number of XRF spectra ('# XRF points') that were collected from each target. The bulk element oxide and element abundances provided were calculated using the PIQUANT software package^{57,65} and have been corrected to remove the effects of diffraction and topographic roughness using the methods described in refs. 15,66.

Where needed to support discussion in the paper or Supplementary Text, the bulk chemical composition of regions of interest (ROIs) within PIXL XRF scans are also shown. These are accompanied by PIXL MCC images that show the locations of the individual PIXL XRF points that are included in the ROI. For all ROIs included in the Supplementary Data Tables, we have also included a list of the PIXL Motion Counter (PMC #s) positions⁵⁷ for each XRF point in the ROI. These PMC locations describe which individual points are included in the ROI.

The element mobility index (τ_{TiO_2}), shown in Fig. 5b, was calculated using the methods described in ref. 67. The calculation of %Fe in vivianite and %Fe in greigite, shown in Fig. 5d, was performed using chemical abundance data for individual PMCs in the 'mudstone' ROIs shown in the Supplementary Data Tables for the targets Apollo Temple, Cheyava Falls, Walhalla Glades, Steamboat Mountain and Malgosa Crest. For each PMC in each mudstone ROI, the Fe and P abundances (in mmol g⁻¹) were combined in a molar Fe:P ratio of 3:2 until all P had been combined with Fe to form vivianite. The individual PMC results for the number of mmol g⁻¹ of Fe in vivianite were then summed and compared with the total abundance of Fe in the mudstone ROI to determine the %Fe in vivianite parameter. In the next step, the remaining Fe in each PMC (after calculation of vivianite abundance) was combined with S in the appropriate molar Fe:S ratio until either all the Fe or all the S had been combined to form greigite. The individual PMC results for the number of mmol g⁻¹ of Fe in greigite were then summed and compared with the total abundance of Fe in the mudstone ROI to determine the %Fe in greigite parameter.

Because PIQUANT assumes that elements are paired with oxygen atoms for the purposes of determining element abundances from the fitting of X-ray spectra, the Fe:S stoichiometry used for estimation of greigite abundance was modified to a value 3:4.42, which differs slightly from idealized greigite stoichiometry (Fe:S = 3:4). The oxide assumption in PIQUANT causes it to overestimate the abundance of S in greigite because it expects the S fluorescence signal to be attenuated by matrix oxygen. To account for this effect, we modelled idealized spectra in PIQUANT for Fe₃S₄ and FeOSO₃ and then determined the ratio of Fe/S K_{α1} fluorescence from each calculated spectrum. PIQUANT correctly reports a 1:1 molar ratio for FeOSO₃. The adjusted greigite stoichiometric ratio was calculated from the Fe/S K_{α1} ratio from Fe₃S₄ divided by the Fe/S K_{α1} ratio from FeOSO₃. The same calculation for the Fe-sulfide minerals troilite (FeS), pyrrhotite (Fe_{0.875}S) and pyrite (FeS₂) yields Fe:S ratios of 1:1.15, 1:1.29 and 1:2.11, respectively.

PIXL diffraction indexing of Ca-sulfate

PIXL has two detectors and so can detect X-ray diffraction from crystalline materials when energies of PIXL's incident radiation happen to be in a diffracting condition with *d*-spacings and orientations of crystal lattices in the target materials^{14,15}. When detected, X-ray diffraction can also be used to assess crystallinity, grain size and grain texture of a target^{14,15,66,68} and to distinguish among minerals with similar elemental compositions^{13,26}. Here diffraction from the Ca-sulfate-rich areas in PIXL scans in Apollo Temple, Walhalla Glades and Steamboat Mountain abrasion patches were compared with modelled diffraction patterns for gypsum, anhydrite and bassanite to identify the most likely mineral phase that matches the observed diffraction as described in detail in ref. 13. A mineral was selected as indexed when the *P* value from the Fisher-transformed cross-correlation results^{13,69} was ≤0.01. Where *P* > 0.01, no mineral was selected as indexed. Owing to the difficulty phasing bassanite¹⁶, beam locations that indexed as bassanite were also treated as not indexed. A summary of the PIXL diffraction results is presented in Supplementary Table 2.

Data availability

The data presented in this paper are available on the NASA Planetary Data System Geoscience Node and Imaging and Cartography Node,

which host dedicated repositories for data derived from the Mars 2020 Rover mission. The DOIs for these repositories are: Mars 2020 Mission bundle, <https://doi.org/10.17189/1522642>; PIXL Instrument bundle, <https://doi.org/10.17189/1522645>; derived data collection for PIXL individual PMC oxide quantifications, <https://doi.org/10.17189/vth5-0676>; RIMFAX Instrument bundle, <https://doi.org/10.17189/1522644>; SHERLOC Instrument bundle, <https://doi.org/10.17189/1522643>; Super-Cam Instrument bundle, <https://doi.org/10.17189/1522646>; Mastcam-Z Science Imaging bundle, <https://doi.org/10.17189/q3ts-c749>; WATSON, ACI, and MCC imager bundle, <https://doi.org/10.17189/1522846>.

Code availability

Quantification of PIXL XRF data was conducted using PIQUANT⁶⁵, a fundamental parameters XRF analysis software package developed for PIXL⁵⁷. PIQUANT is embedded in the data visualization software package called PIXLISE^{57,70,71}, which was used for analysis of quantified PIXL XRF data. The PIXLISE and PIQUANT software packages can be accessed at [PIXLISE.org](https://pixlise.org). PIXLISE source code versions are archived for reproducibility at OFS.io⁷².

56. Hamran, S. E. et al. Radar Imager for Mars' Subsurface Experiment—RIMFAX. *Space Sci. Rev.* **216**, 128 (2020).
57. Allwood, A. C. et al. PIXL: Planetary Instrument for X-ray Lithochemistry. *Space Sci. Rev.* **216**, 134 (2020).
58. Maurice, S. et al. The SuperCam instrument suite on the Mars 2020 rover: science objectives and mast-unit description. *Space Sci. Rev.* **217**, 47 (2021).
59. Wiens, R. C. et al. The SuperCam instrument suite on the NASA Mars 2020 rover: body unit and combined system tests. *Space Sci. Rev.* **217**, 4 (2021).
60. Bell, J. F. et al. The Mars 2020 Perseverance rover Mast Camera Zoom (Mastcam-Z) multispectral, stereoscopic imaging investigation. *Space Sci. Rev.* **217**, 24 (2021).
61. Moeller, R. C. et al. The Sampling and Caching Subsystem (SCS) for the scientific exploration of Jezero Crater by the Mars 2020 Perseverance rover. *Space Sci. Rev.* **217**, 5 (2020).
62. Sharma, S. et al. Diverse organic-mineral associations in Jezero Crater, Mars. *Nature* **619**, 724–72 (2023).
63. Osterhout, J. T., Schopf, J. W., Kudryavtsev, A. B., Czaja, A. D. & Williford, K. H. Deep-UV Raman spectroscopy of carbonaceous Precambrian microfossils: insights into the search for past life on Mars. *Astrobiology* **22**, 1239–1254 (2022).
64. Jakubek, R. S. et al. Spectral Background Calibration of Scanning Habitable Environments with Raman and Luminescence for Organics and Chemicals (SHERLOC) spectrometer onboard the rover enables identification of a ubiquitous Martian spectral component. *Appl. Spectrosc.* <https://doi.org/10.1177/00037028241280081> (2024).
65. Heirwegh, C. M., Elam, W. T., O'Neil, L. P., Sinclair, K. P. & Das, A. The focused beam X-ray fluorescence elemental quantification software package PIQUANT. *Spectrochim. Acta Part B* **196**, 106520 (2022).
66. Schmidt, M. E. et al. Diverse and highly differentiated lava suite in Jezero Crater, Mars: constraints on intracrustal magmatism revealed by Mars 2020 PIXL. *Sci. Adv.* **11**, eadr2613 (2025).
67. Chadwick, O. A., Brimhall, G. H. & Hendricks, D. M. From a black to a gray box—a mass balance interpretation of pedogenesis. *Geomorphology* **3**, 369–390 (1990).

68. Liu, Y. et al. An olivine cumulate outcrop on the floor of Jezero Crater, Mars. *Science* **377**, 1513–151 (2022).
69. Fisher, R. A. Frequency distribution of the values of the correlation coefficient in samples from an indefinitely large population. *Biometrika* **10**, 507–521 (1914).
70. Wright, A. P., Nemere, P., Galvin, A., Chau, D. H. & Davidoff, S. Lessons from the development of an anomaly detection interface on the Mars Perseverance Rover using the ISHMAP framework. In *Proc. 28th International Conference on Intelligent User Interfaces* 91–105 (Association for Computing Machinery, 2023).
71. Schurman, D. et al. PIXELATE: novel visualization and computational methods for the analysis of astrobiological spectroscopy data. In *AbSciCon 2019*, 401–8 (American Geophysical Union, 2019).
72. Davidoff, S. et al. PIXLISE spectroscopy analysis software: released versions for published analyses. *OSF* <https://doi.org/10.17605/OSF.IO/URE2F> (2024).

Acknowledgements We acknowledge the efforts of the Mars 2020 Science and Engineering Teams. This work was carried out by A.C.A., M.L.C., K.P.H., K.U., S.D., K.A.F., S.W.L., Y.L., K.M.S., L.A.W., C.M.H. and J.N.M. at the Jet Propulsion Laboratory, California Institute of Technology, under a contract with the National Aeronautics and Space Administration (80NMO018D0004).

Author contributions Conceptualization: A.C.A., S.B., A.B., A.P.B., K.A.F., D.T.F., B.G., S.G., K.P.H., J.A.H., M.S.R., E.S., M.E.S., M.D.S., D.L.S., K.M.S., M.M.T., A.H.T., K.U., R.C.W. and K.H.W. Methodology: J.F.B., O.B., R. Bhartia, E.A.C., D.T.F., B.G., S.-E.H., K.P.H., J.A.H., J.R.J., M.W.M.J., Y.L., L.M., L.P.O'N., M.S.R., P.R., E.S., A. Steele, M.M.T., K.U., S.J.V., L.A.W., B.P.W. and K.H.W. Software: S.D., D.T.F., T. Fouchet, S.-E.H., P.S.J., D.A.K., L.P.O'N., G.P., E.S., S. Sharma, M.M.T., K.U., S.J.V. and K.H.W. Validation: J.A.H., J.R.J., E.S., M.M.T., L.A.W. and K.H.W. Formal analysis: A.C.A., E.L.C., E.D., T. Fornaro, K.P.H., J.A.H., M.W.M.J., H.K., L.P.O'N., B.J.O., M.S.R., E.S., S. Siljeström, A. Steele, M.M.T., K.U., S.J.V. and K.H.W. Investigation: R. Barnes, A.B., P.B., K.B., S.B., O.B., R. Bhartia, T.B., A.J.B., A.P.B., G.C., E.L.C., E.C., E.A.C., A.C., E.D., K.A.F., D.T.F., T. Fornaro, T. Fouchet, B.G., S.G., S.-E.H., K.P.H., K.H.-L., J.A.H., J.R.J., A.J.J., M.W.M.J., P.S.J., L.C.K., H.K., T.V.K., D.A.K., S.W.L., A.Y.L., Y.L., J.N.M., L.M., N.M., J.A.M., J.M.-F., E.L.M., A.E.M., J.I.N., L.P.O'N., B.J.O., D.A.P., C.Q.-N., M.S.R., P.R., E.S., M.E.S., M.D.S., S. Sharma, D.L.S., K.L.S., S. Siljeström, J.I.S., K.M.S., A. Steele, M.M.T., A.H.T., K.U., S.J.V., L.A.W., B.P.W., R.C.W., K.H.W. and B.V.W. Resources: J.F.B., A.P.B., M.L.C., K.P.H., J.A.H., S.W.L. and D.A.P. Data curation: P.A.B., A.B., J.F.B., E.L.C., S.D., B.G., C.M.H., J.E.H., H.K., J.N.M., J.A.M., E.L.M., G.P., A.C.P., N.P., M.S.R., A.H.T., K.U., S.J.V., B.V.W. and Z.U.W. Writing—original draft: A.C.A., E.L.C., E.D., F.G., S.G., J.A.H., M.S.R., L.A.W. and R.C.W. Writing—review and editing: R. Barnes, P.B., K.B., S.B., O.B., R. Bhartia, T.B., A.B., A.P.B., M.L.C., G.C., E.L.C., E.C., E.A.C., E.D., A.G.F., D.T.F., T. Fornaro, T. Fouchet, F.G., S.G., K.P.H., E.M.H., C.D.K.H., K.H.-L., J.A.H., J.R.J., A.J.J., M.W.M.J., P.S.J., L.C.K., T.V.K., D.A.K., A.Y.L., Y.L., L.M., N.M., J.A.M., J.M.-F., F.M.M., E.L.M., A.E.M., J.I.N., L.P.O'N., B.J.O., C.Q.-N., M.S.R., P.R., M.E.S., M.D.S., S. Sharma, D.L.S., K.L.S., S. Siljeström, J.I.S., A. Srivastava, K.M.S., A. Steele, M.M.T., N.J.T., A.H.T., K.U., S.J.V., L.A.W., B.P.W., R.C.W. and K.H.W. Visualization: R. Barnes, P.A.B., A.B., J.F.B., E.L.C., E.C., S.D., E.D., B.G., S.-E.H., J.E.H., J.A.H., J.R.J., M.W.M.J., P.S.J., J.L.J., D.A.K., J.N.M., J.M.-F., G.P., A.C.P., N.P., M.S.R., P.R., M.M.T., K.U. and S.J.V. Supervision: J.F.B., M.L.C., A.C., K.A.F., S.G., K.P.H., J.A.H., J.R.J., J.L.J., S.W.L., J.N.M., M.D.S., K.M.S., M.M.T., K.U. and R.C.W. Project administration: J.F.B., M.L.C., A.C., K.A.F., T. Fouchet, S.-E.H., K.P.H., J.A.H., J.L.J., L.C.K., S.W.L., J.N.M., D.A.P., M.D.S., K.M.S. and R.C.W. Funding acquisition: A.C.A., J.F.B., M.L.C., T. Fouchet, S.G., K.P.H., J.A.H., J.L.J., S.W.L., D.A.P. and R.C.W.

Competing interests The authors declare no competing interests.

Additional information

Supplementary information The online version contains supplementary material available at <https://doi.org/10.1038/s41586-025-09413-0>.

Correspondence and requests for materials should be addressed to Joel A. Hurowitz.

Peer review information *Nature* thanks Janice Bishop, Aude Picard and the other, anonymous, reviewer(s) for their contribution to the peer review of this work. Peer reviewer reports are available.

Reprints and permissions information is available at <http://www.nature.com/reprints>.